Regulating Reactive Oxygen Intermediates of SAzyme via Second-Shell coordination for Selective Aerobic Oxidation

Yuan Xu[a], Yuanjie Ma[b], Xinghua Chen[a], Kaiqing Wu[a], Kaiyuan Wang[a], Yanfei Shen[a], Songqin Liu[a], Xuejiao J. Gao*[b], Yuanjian Zhang*[a]

[a] Jiangsu Engineering Laboratory of Smart Carbon-Rich Materials and Device, Jiangsu Province Hi-Tech Key Laboratory for Bio-Medical Research, School of Chemistry and Chemical Engineering, Medical School, Southeast University, Nanjing 211189, China, Email: Yuanjian.Zhang@seu.edu.cn.

[b] College of Chemistry and Chemical Engineering, Jiangxi Normal University, Nanchang 330022, China, Email: gaoxj@jxnu.edu.cn.

Abstract

Reactive oxygen species (ROS) regulation for artificial oxidoreductase is a key scientific issue that determines the activity, selectivity, and stability of aerobic reaction. However, the poor understanding of ROS formation mechanism greatly hampers their wider deployment. Herein, inspired by cytochromes P450 affording bound ROS intermediates in O_2 activation, we report single-atom FeN_4 site with tunable second-shell anion could regulate ROS generating pathways. Remarkably, the second-shell S anion coordinated FeN_4 (denoted as FeNSC) delivers 2.4-fold higher oxidase-like activity and only 17% free ROS generation compared to FeNC. The detailed XANES analysis and DFT calculations reveal that the second shell S-doping significantly altered the electronic structure of FeN_4 sites, leading to an increase of electron density at Fermi level and the enhanced electron transfer from active sites to the key intermediate *OOH, thereby determining the type of ROS in aerobic oxidation process. FeNC with different second-shell anion were further applied to drive aerobic oxidation reaction with enhanced activity, selectivity, and stability.

Introduction

Free reactive oxygen species (ROS), such as $^1O_2$, •OH, $•O_2^-$, and H_2O_2, have been widely known as powerful aqueous redox species since the concentration of atmospheric O_2 from Great Oxidation Event. All living organisms except for few anaerobic and aerotolerant species, need O_2 to preserve life.[1, 2] For instance, mitochondria in eukaryotic cells or cell membranes in bacteria drive the aerobic generation of chemical energy, along with the release of electrons to O_2 through electron transport chains to form free ROS.[3] For the same reason, free ROS have demonstrated extensive applications in biological, chemical and environment fields by virtue of their relative high reaction activity.[4] However, obscure understanding of free ROS formation mechanism greatly hampers their wider deployment. For instance, owning to the toxic nature and indiscriminate activity of excessive free ROS, the livings have suffered from oxidative-stress disease,[5, 6] and industrial reactions involving uncontrollable free ROS would proceed at the expense of greatly compromising catalytic selectivity and stability.[7, 8] Hence, exploring the mystery of free ROS formation to manipulate reaction activity, selectivity, and stability is highly envisioned.

Along this line, extrinsic efforts such as by changing irradiation light[9, 10] and loading specific radical scavengers[7] but also intrinsic structure engineering of catalysts in disclosure of the rules of free ROS generation have been made.[11, 12] For instance, atomically dispersed single-atom catalysts (SACs) that are highly uniform active centers, tunable coordination environment and high atom utilization efficiency, have offered a fundamental platform to explore insights of free ROS formation.[13-19] Among them, Fe–N–C containing atomically dispersed FeN_4 moieties receive ever-increasing attention due to maximized atom utilization and desired activity.[20-23] The activity origin of FeN_4 moieties to activate oxygen or its derived intermediates have been partially identified from

free ROS, including $^1O_2$, •OH, and $•O_2^-$,[24-28] while some evidence points to the formation of bound ROS (high-valent metal−oxo species).[29-32] Therefore, the significant impacts of FeN_4 sites electron structure on the formation of ROS is still the subject of extensive debate. Moreover, whether or to what extent can the electronic configuration of active sites influence the formation of free ROS remains elusive.

Millions of years of the ingenious evolution bring in the refined hierarchical structures of cytochromes P450 (CYPs). They are capable of effective activating O_2 to afford metal-oxygen intermediates with negligible free ROS release.[33-36] Inspired from their refined tetrapyrrolic FeN_4 active sites and S-containing ligand (cysteine), here, we report a proof-of-concept evaluation of the electronic configuration for FeN_4 sites with S functionalization on the formation of active oxygen species. Interestingly, Fe–N–C with discriminating tetrapyridinic FeN_4 and second-shell S anion tetrapyrrolic FeN_4 sites, demonstrated different pathways of active oxygen species generation on FeN_4 sites. The detailed XANES analysis and DFT calculations revealed that the second shell S-doping significantly altered the electronic structure of FeN_4 sites, leading to an increase of electron density at Fermi level and the enhanced electron transfer from active sites to the key intermediate *OOH, thereby determining the type of ROS in aerobic oxidation process. This study not only provides a new perspective of understanding free ROS formation but also highlights the influence of intrinsic electronic environment in activating oxygen by FeN_4 active sites.

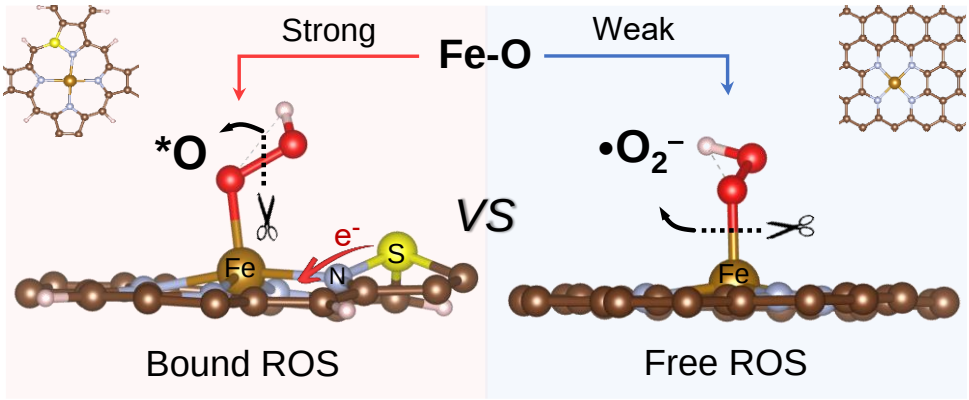

Scheme 1. Scheme for regulating reactive oxygen intermediates of Fe-N_4 SAzyme via second-shell coordination.

Results and discussion

Structure characterizations of Fe–N–C.

In this study, FeNSC and FeNC were synthesized via a polymerization-pyrolysis combined strategy using O-phenylenediamine (OPD) and $FeCl_3 \cdot 6H_2O$ as precursors. Ammonium persulfate and hydrogen peroxide were used as polymerization initiator upon the polymerization stage respectively. As shown in Figure S1, the transmission electron microscopy (TEM) images of both FeNC and FeNSC disclosed the onion-like graphitic shells. No obvious Fe/FeO nanoparticles existed on the surface of all these samples, which were consistent with the XRD results that without any diffraction peaks assigning to crystalline Fe species (Figure S2). Moreover, high-angle annular darkfield scanning transmission electron microscopy (HAADF-STEM) images in Figure 1b, c showed that Fe was atomically dispersed within the carbon surface (dots exhibiting bright contrast), indictive of similar microstructure among FeNC and FeNSC exhibiting single Fe atoms and graphene-type matrix. The corresponding EDS mapping further suggested the homogeneous distribution of Fe species over FeNSC (Figure 1d) and FeNC (Figure S3).

To probe the surface chemical compositions and bonding information, X-ray photoelectron spectroscopy (XPS) was first utilized. As depicted in Figure S4, the XPS survey spectra verify the existence of C, N, Fe in all samples. Compared to FeNC, a new peak located at ~ 163 eV was observed in FeNSC, which was attributed to S 2p. The S 2p peak could be deconvoluted into two pairs of peaks, in which the dominant S species around 164.0 eV and 165.3 eV were mainly assigned to the $2p_{3/2}$ and $2p_{1/2}$ of thiophenic S; The peak at 167.5 eV and 169.0 eV were ascribed to the oxidized S group (Figure 1e).[37] Additionally, compared with the sample without acid-wash treatment, the absence of the characteristic peak of Fe-S bond suggested that the exotic S atoms tended to bond to surrounding C atoms to form C-S-C structure rather than bonding to the central Fe atoms (Figure S5).[38] These results suggest that sulfur atoms were successfully incorporated into the graphitic carbons.

The N 1s spectrum of FeNSC in Figure 1e could be deconvoluted into five peaks, assigning to pyridinic N (398.4 eV), N_x-Fe (399.4 eV), pyrrolic N (400.2 eV), graphitic N (401.3 eV), and oxidized N (403.0 eV).[39] Notably, as demonstrated in Figure 1f and Table S1, the atomic percentages of pyrrolic N in FeNSC (1.39 %) was significantly higher than that in FeNC (0.45 %), indicating the doping of S element can favor the formation of pyrrolic N species.[40-42] Notably, the N 1s peak of FeNSC shifted towards a lower binding energy direction compared to that of FeNC, implying a partial electron transfer from S to N. Besides, the Raman spectra showed that the intensity ratio between D-band (~ 1350 cm^{-1}, disordered sp^3 carbon) and G band (~ 1595 cm^{-1}, graphitic sp^2 carbon) for FeNC was ca. 1.27, which was small than FeNSC, indicating the introduction of sulfur brings more defects (Figure S6). These results jointly illustrated that the introduction of S increased not only the degree of defects but also the content of pyrrolic N on both an absolute and relative basis (Figure 1g).

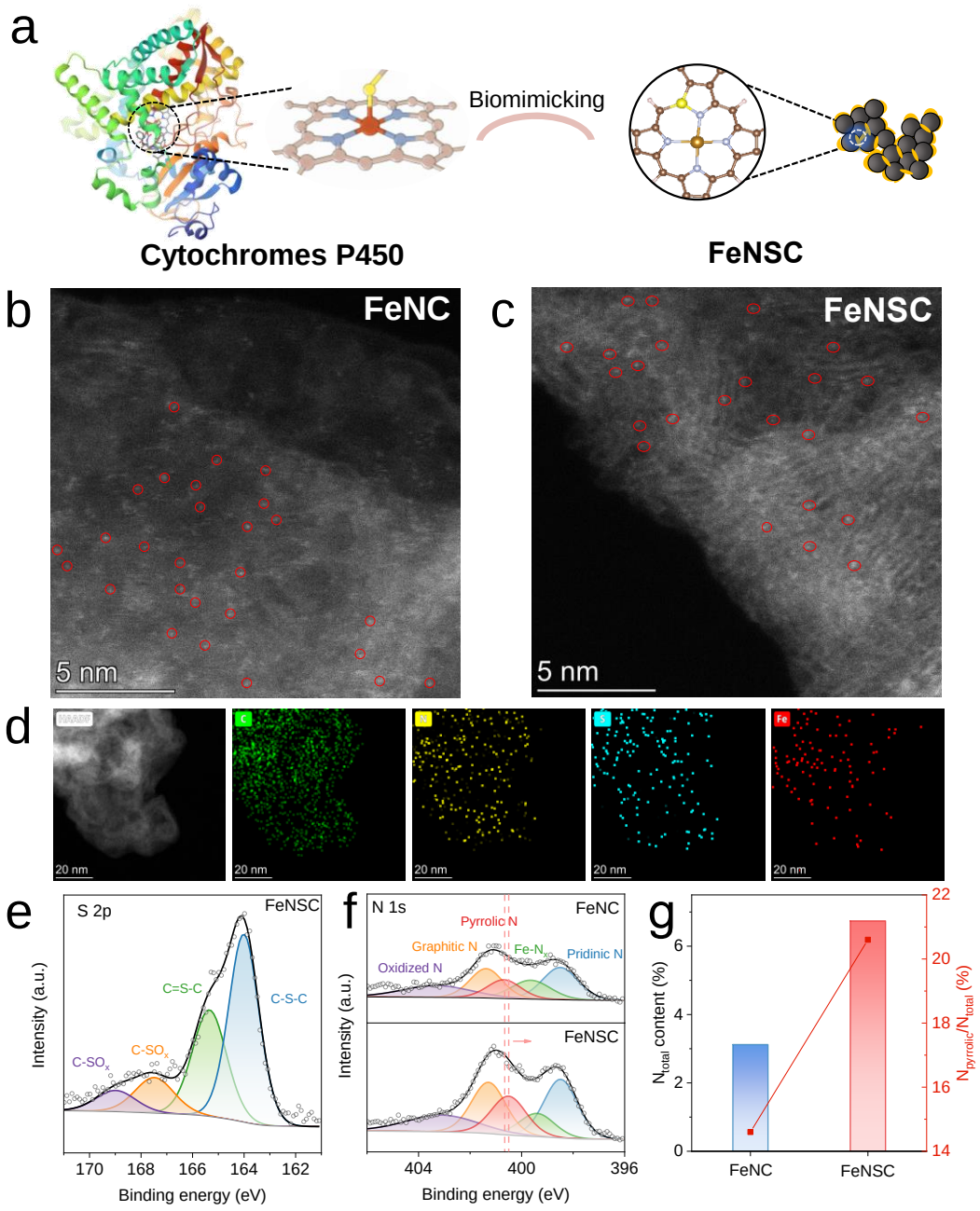

Figure 1. (a) Biomimetic construction of FeNSC by mimicking the tetrapyrrolic FeN_4 active sites and S-containing ligand of CYP. HAADF-STEM images of (b) FeNC and (c) FeNSC. (d) HAADF-STEM EDS mapping images of FeNSC showing the elemental distribution of C, N, S, and Fe. (e) High resolution S 2p XPS spectra of FeNSC. (f) High resolution N 1s XPS spectra of FeNC and FeNSC. (g) the content of total nitrogen and pyrrolic nitrogen determined by N 1s XPS analysis.

To further distinguish the chemical states and local coordination environment of atomically dispersed Fe species, Fe K-edge X-ray absorption near-edge structure (XANES) and Fourier transform extended X-ray absorption fine structure (FT-EXAFS) spectra were measured. The XANES profiles of all samples and references were normalized in a first step, the detailed energy range from 7100 to 7200 eV was demonstrated in Figure 2a, suggesting the predominance of Fe^{3+} in FeNSC. Electron paramagnetic resonance (EPR) spectra in Figure 2c also corroborated the stronger signal of high-spin ferric iron species in FeNSC than FeNC observed at g factor of 4.25. Besides, the pre-edge peak at 7115 eV in FePc, assigning to Fe(1s) → Fe−ligand(π*) quadrupolar transition with simultaneous ligand-to-metal charge transfer was observed in FeNSC, as the fingerprint of square-planar tetrapyrrolic Fe–N_4 motif (D_4h symmetry)[29], whereas inconspicuous peak at 7115 eV was observed for FeNC, indicating that the FeNSC contains a similar tetrapyrrolic D_{4h} configuration with FePc (Figure 2d).

The characteristic peaks in Fe K-edge XANES, ascribing to the multiple electron-scattering process were further analyzed. As shown in Figure 2b, well-defined peaks at 7133 (A) and 7148 eV (C) were observed for FeNSC, while at the same region only a relative board peak at 7135 eV (B) was noted for FeNC, indicating FeNSC had a more diversified interaction between Fe and neighboring atoms on first/second/third shells. The shape and energy of peak D are related to the spin state of Fe atom, and its energy is highly related to the bond length of the metal and nitrogen atom at first coordination shell.[43] The lower D peak energy of FeNSC (7178 eV) revealed a longer bond length of Fe-N compared with FeNC (7188 eV) according to the Natoli rule (Ed^2 = constant, where E is the peak energy relative to a given zero energy and d is the mean bond length).[44] These results indicated that the introduction of sulfur element significantly enriched the interaction between central Fe atom and neighboring atoms.

K^3-weighted Fourier-Transformed-EXAFS was then investigated to derive the detailed structural information on the local coordination geometry of Fe. As depicted in Figure 2g, the predominant peaks at ~1.5 Å for FeNC and FeNSC could be attributed to the Fe−N scattering path (without phase correction). The Fe-Fe metallic path at ~2.2 Å was absent, revealing the atomical dispersion of Fe in both FeNC and FeNSC, in agreement with the above TEM and XRD results. An additional peak appeared at 2.5 Å in FeNSC is akin to the second-shell Fe-C scattering in Fe phthalocyanine (FePc).[45] Considering the different type of coordination N in XPS N1s spectra and the position of FeNSC was closer to that of FePc from Fe K-edge XANES, FeNC may dominate the pyridinic Fe-N structure, while the FeNSC mainly consisted of the pyrrolic Fe-N structure.

To further reveal the exact coordination states of Fe center, the EXAFS curve fitting assessments were conducted. The first coordination shell for both FeNC and FeNSC could be fitted by a Fe-N scattering path with a Fe-N coordination number of four. Moreover, the Fe K-edge EXAFS of FeNC in both *k* space and *R* space fitted well with the proposed models of tetrapyridinic FeNC (Figure 2e, f). While the Fe K-edge EXAFS of FeNSC showed a better fitting result when using tetrapyridinic FeNSC model (Figure 2h, i, Table S2, S3). From these characterizations, the rationality of the FeN_4 configuration in FeNC with a tetrapyridinic structure, and the FeN_4 configuration in FeNSC with a second-shell S-doped tetrapyrrolic structure are confirmed.

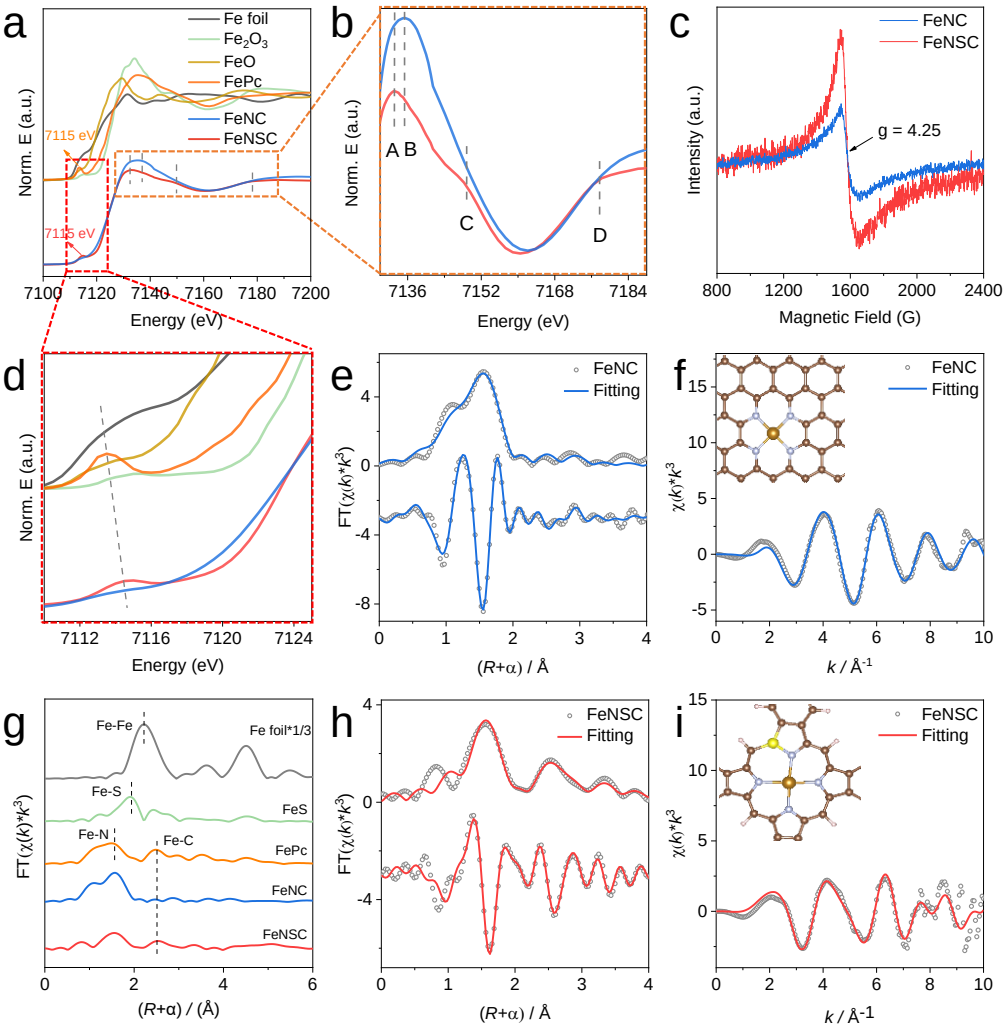

Figure 2 (a) Experimental Fe K-edge XANES spectra of FeNC, FeNSC and reference samples. (b) Detailed experimental Fe K-edge XANES spectra of FeNC and FeNSC ranging from 7130 to 7188 eV. (c) Electron paramagnetic resonance (EPR) spectra of FeNC and FeNSC measured at 100 K. (d) Detailed experimental Fe K-edge XANES spectra of FeNC and FeNSC ranging from 7110 to 7125 eV. (g) k^3-weighted Fourier-transformed χ χ(k)-function of the experimental Fe K-edge EXAFS signal of FeNC and FeNSC along with reference samples. Fe K-edge EXAFS (points) and the curve fitting (line) for (i) FeNC and (h) FeNSC shown in R-space (FT magnitude and imaginary component). The data are k^3-weighted without phase correction. Fe K-edge EXAFS (points) and the curve fitting (line) for (f) FeNC and (i) FeNSC shown in k^3-weighted k-space. Inset in (f) and (i) are the proposed models for FeNC and FeNSC, respectively.

Different active oxygen species generation in oxidase-like activity of FeNC and FeNSC

In the first set of experiments, to determine the oxygen activation performance of FeNC and FeNSC, 3,3',5,5'-tetramethylbenzidine (TMB) was selected as a colorimetric substrate, which has been widely used to valuate the ability of catalysts to activate oxygen or hydrogen peroxide molecule in biomimetic environment due to its convenient colorimetric readout. The oxidation product of TMB could be assayed at 652 nm ($\varepsilon_{652\ nm}$= 39,000 M^{-1} cm^{-1}) using UV-vis spectrometer (Figure 3a).[46] Furthermore, the initial velocities of TMB oxidation were calculated via the Beer–Lambert law, and were then plotted and fitted well with Michaelis–Menten curves. To obtain the maximum velocity (ν_{max}), a linear double reciprocal plot (Lineweaver–Burk plot) was applied as given in Figure 3b and Figure S7. These results suggested, the FeNSC exhibited a much higher oxidase-like activity towards TMB (ν_{max} =0.38 μM s^{-1}) compared to FeNC (ν_{max} =0.16 μM s^{-1}).

To confirm the active sites in Fe-N-Cs for activating oxygen, SCN^- was used as the probe to coordinate with Fe.[47] It was found that all the Fe-N-Cs were irreversibly inhibited by SCN poison (Figure S8), confirming that Fe-N_4 moieties was the active sites of both tetrapyridinic and tetrapyrrolic FeN_4 for driving the oxygen activation process.

Next, to clarify the active species during oxygen activation process of Fe-N-Cs, free ROS were detected by EPR using 5,5-diemthyl-1-pyrroline N-oxide, DMPO. As shown in Figure 3c, the six characteristic peaks for typical DMPO-$O_2^{\bullet-}$ adducts in an acidic environment was observed only for FeNC.[48] Other possible active species such as singlet oxygen ($^1O_2$) and •OH were also examined by EPR (Figure S9), and no characteristic signals were detected for both FeNC and FeNSC. Chemical trapping agent (furfuryl alcohol for $^1O_2$,[49] mannitol for •OH, and superoxide dismutase for $\bullet O_2^-$ [50]) were also employed

to quantity free ROS. For this, the time-dependent UV-vis absorbance of TMB oxidation product at 652 nm was recorded after adding chemical trapping agents. It was found FeNSC had negligible activity loss compared with FeNC, and ca. 0.86 μM of steady-state $\bullet O_2^-$ was calculated for FeNC, while only ca. 0.15 μM steady-state $\bullet O_2^-$ for FeNSC under the same detection condition (Figure 3d). These results revealed that FeNSC exhibited significantly fewer generation of $\bullet O_2^-$ during TMB oxidation.

It is worth noting that the tetrapyrrolic $M-N_4$ structure is ubiquitously present in nature. For example, tetrapyrrolic $Fe-N_4$ motifs constitute the active sites of heme-containing enzymes. In mammal's blood, tetrapyrrolic $Fe-N_4$ motifs in heme play an indispensable role in binding oxygen. For instance, cytochrome P450 enzymes active molecule oxygen on a manner of high-valent $Fe^{IV}=O$ intermediate (bound ROS pathway) with negligible free ROS release.[34, 35, 51] Thus, to disclose whether FeNC or FeNSC generated an $Fe^{IV}=O$ intermediate resemble heme-containing enzymes, EPR spectroscopy in the solid-state at low-temperature (100 K) was undertook. As shown in Figure 3e, a representative peak only occurred in FeNSC with a rhombic signal at g factor ≈ 2, consistent with η^2-peroxo heme species, confirming the existence of $Fe^{IV}=O$ intermediate in FeNSC (bound ROS).[29, 52] Furthermore, after reaction with the substrate TMB, FeNSC revealed a much more intense signal of $Fe^{IV}=O$ than that of FeNC, indicating the vigorous participation of $Fe^{IV}=O$ in the catalytic process of FeNSC (Figure 3f).

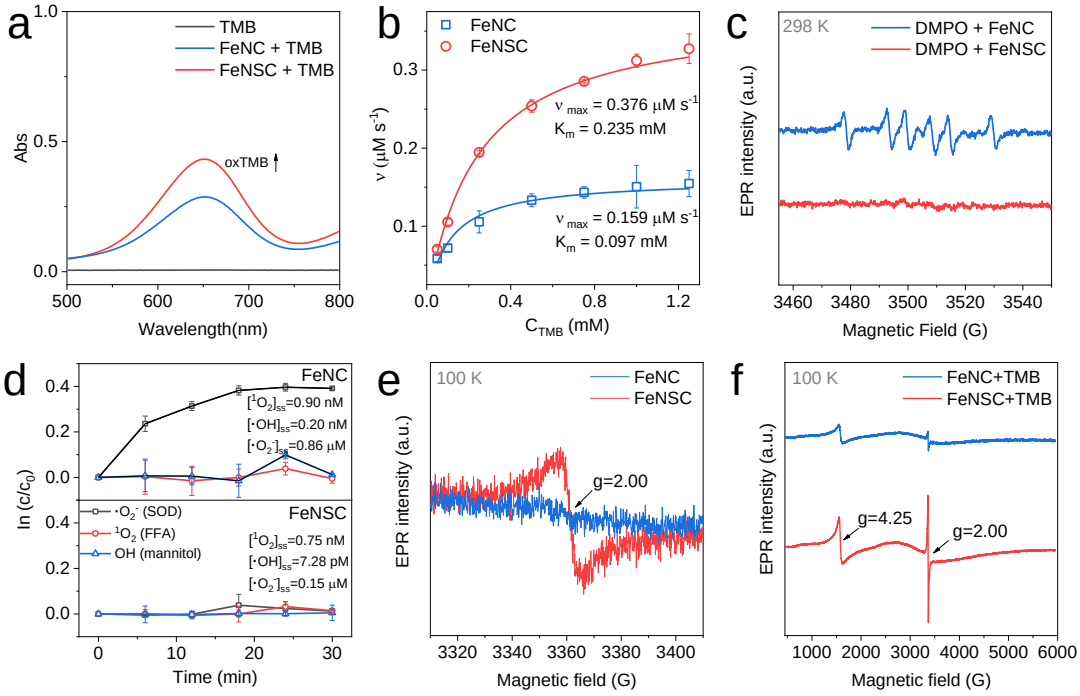

Figure 3 Different active oxygen species generation on FeN_4 sites during substrate oxidation. (a) UV-vis absorption for TMB oxidation in the presence of FeNC and FeNSC. (b) Michaelis–Menten steady-state kinetics curves for FeNC and FeNSC. (c) EPR spectra of DMPO-•O_2^- adduct generated by FeNC and FeNSC measured at 298 K in air-saturated NaAc-HAc buffer solution (d) Steady-state concentration of $^1O_2$, •OH, and •O_2^- calculated from the decay of TMB oxidation product accumulation over time after the addition of different scavengers. Solid-state EPR spectra of FeNC and FeNSC at 100 K (e) before and (f) after reaction with TMB.

Density Functional Theory (DFT) calculations

Considering that FeNSC and FeNC had remarkably different intermediate states, DFT calculations were performed to interpret the catalytic path of free ROS release and bound ROS formation during oxidation. The first observation pertains to the significant enhancement of oxidase-like activity in FeNC upon sulfur doping. More crucially, the second observation involves a distinct mechanism of ROS generation during oxidation processes. It was noted that

sulfur-doped FeNSC markedly diminishes free ROS production compared to undoped FeNC.

To simulate the FeNC and FeNSC materials, four periodic structural models, as depicted in Figure 4a, were employed. These models were informed by experimental characterizations indicating an increase in five-membered ring structures due to sulfur doping. Furthermore, considering the electron donation of nitrogen atoms perpendicular to the conjugation plane, which imparts aromatic stabilization to the five-membered ring, we developed the **FeNSC1** and **FeNSC2** models. These models feature distinct coordination environments compared to **FeNC1**, with the sulfur dopant positioned in para- and meso-positions relative to iron, respectively. Additionally, to assess the impact of coordination environment on the catalytic efficacy of the central iron atom, the **FeNC2** model was introduced for comparative analysis. The FeN_4 sites were identified as the active sites. The study investigated both four- and two-electron oxidation processes of TMB by O_2, leading to the formation of H_2O and H_2O_2, respectively. The proposed mechanisms, encompassing elementary reactions and key intermediates for the four- and two-electron oxidation processes are presented in Figure 4b and Figure S10a, respectively. Energy profiles were computed, highlighting the steps with the highest energy barriers and their corresponding energy values, which are annotated in the profiles.

The energy profile analysis reveals that for both the four-electron (Figure 4b) and two-electron (Figure S10a) reduction processes, the **FeNSC2** model exhibits a notably steeper potential energy surface. This is coupled with a markedly enhanced adsorption affinity for the reactant O_2 and various intermediates, in comparison to the other three models studied. Despite the final *OH desorption step (* denoting the adsorbed state) being an energetically uphill process, requiring as much as 2.15 eV, the adsorption energy of **FeNSC2** for O_2 is also significantly high, reaching up to 2.09 eV. This suggests a substantial likelihood of competitive adsorption taking place, which is

instrumental in facilitating the completion of the catalytic cycle. These computational findings align well with the experimental observations, which indicate that the FeNSC materials demonstrate superior catalytic reaction rates and heightened activities compared to their FeNC counterparts.

The comparative analysis of reaction curves for **FeNC1** and **FeNC2** indicates that variations in the Fe atomic coordination environment exert minimal influence on catalytic activity. Instead, the notable enhancement in both the catalytic activity and mechanism observed in **FeNSC2** is primarily attributed to sulfur doping, rather than alterations in the coordination environment. Further comparison between **FeNSC1** and **FeNSC2** underscores that sulfur positioned in the Fe interstitial site, as opposed to the para position, significantly bolsters oxidase activity while concurrently suppressing the generation of free ROS. Consequently, it is deduced that the localized structure in **FeNSC2** more accurately mirrors the structure synthesized experimentally, as opposed to that in **FeNSC1**. This conclusion is corroborated by the closer alignment of the FT-EXAFS curves, modeled on **FeNSC2**, with the experimental characterization results (Figure 2i).

Computational analyses further reveal that **FeNSC2** demonstrates markedly stronger adsorption for a variety of ROS intermediates, including O_2, H_2O_2, *OOH, OH, and O (as shown in Figure S10b). This finding elucidated the experimental observation of FeNSC materials significantly reducing the production of free ROS. Additionally, while the dissociation of O-O bonds to yield O* (the four-electron reduction) from adsorbed *OOH on the surfaces of the four models are exergonic processes, the cleavage of Fe-O bonds leading to H_2O_2 formation (the two-electron reduction) are also endergonic reactions. Despite this, all four models demonstrate enhanced selectivity for the four-electron reduction pathway. Notably, **FeSCN2** exhibits a substantial increase in H_2O_2 adsorption, significantly elevating the chance of H_2O_2 engaging in a reverse reaction to generate *OOH and thus completing the four-electron

reduction cycle. Consequently, **FeSCN2** is distinguished by its superior selectivity for the four-electron reduction process. Conversely, the other three materials, particularly **FeNC1** and **FeNC2**, are characterized by relatively uniform potential energy landscapes and decreased absolute adsorption energies for ROS, leading to diminished selectivity and a heightened propensity for the inadvertent release of ROS.

To further understand these outcomes, the band structures and projected density of states (PDOS) of the four models were examined, with the results presented in Figure 4c. Notably, the *d*-band centers of the central Fe atom were highlighted in the PDOS panels. These results indicate that S doping alters the band structure, leading to the emergence of flat bands in both **FeNSC1** and **FeNSC2**. Electrons in these flat bands traverse the material more slowly compared to those in bands with a steeper slope, resulting in a higher density of electronic states at the Fermi level. This increased density facilitates the material's participation in redox reactions due to the greater availability of electrons for transfer. Consequently, these findings elucidate why **FeNSC2** exhibits higher catalytic activity and stronger interactions with ROS, as more flat bands are present in its energy band structure. Additionally, the highest *d*-band center in **FeNSC2** further supports its robust interaction with ROS.

The investigation of electronic effects was furthered by analyzing the differential charge density ρ_{def}. This was achieved through the calculation of $\rho_{def,Fe}$ and $\rho_{def,OOH}$, utilizing the following equations:

$$\rho_{def,Fe} = \rho_{FeNC} - (\rho_{Fe} + \rho_{NC}) \quad (1)$$

$$\rho_{def,OOH} = \rho_{OOH^*} - (\rho_{OOH} + \rho_{slab}) \quad (2)$$

where ρ_{FeNC}, ρ_{Fe}, ρ_{NC}, ρ_{OOH^*}, ρ_{OOH} and ρ_{slab} are electronic densities of Fe–N–C, Fe atom, NC substrate, adsorbed OOH with slab, free OOH and the bare slab.

It is found that S atoms, particularly in the **FeNSC2** model, exhibit electron-donating properties, as evidenced by the differential charge on S being –0.72.

Notably, this electron donation does not compromise the electropositivity of the central Fe atom, which is maintained due to its stable coordination with four pyrrole rings. The calculated $\rho_{def,OOH}$ for **FeNSC2** indicates a net charge density increase of 0.54 on the OOH group, while the Fe atom experiences the most significant charge density decrease of −1.47. This suggests that the electron-donating effect of the S atom facilitates electron transfer from the substrate to the adsorbed OOH, thereby enhancing electrostatic interactions.

In these regards, the incorporation of S atoms in the second-shell coordination markedly influences the catalytic activity and mechanism of FeN_4 centers, with their positional placement proving critical. Notably, the interstitial position of S atoms relative to Fe atoms is more advantageous than the para position. The electron-donating nature of the S atom plays a pivotal role in modulating the energy band structure of Fe–N–C. This modulation not only strengthens the interaction between the substrate and ROS but also concurrently amplifies the catalytic activity. Thus, the regulation of ROS could be achieved by introducing interstitial position S atom in FeN_4 second-shell coordination.

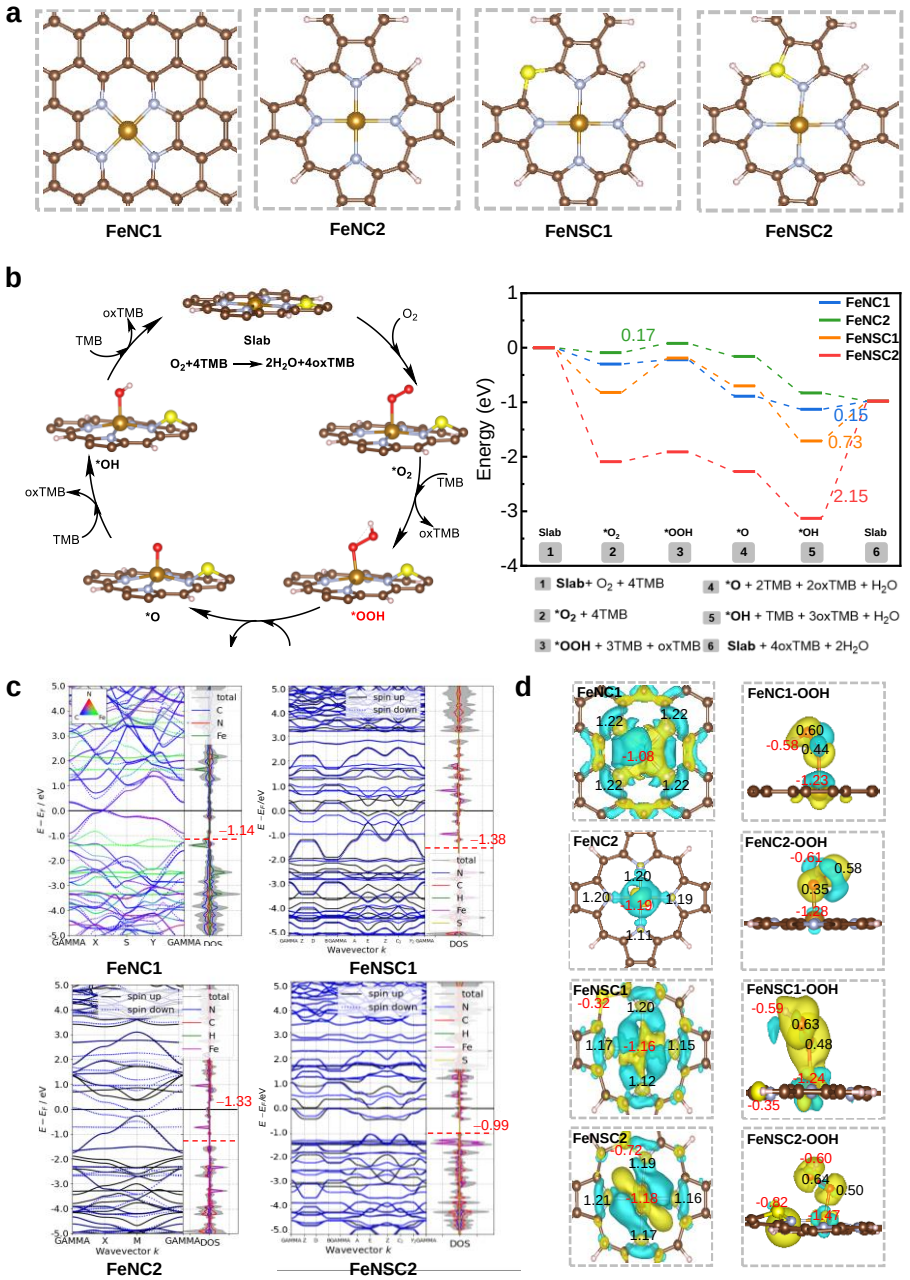

Figure 4. (**a**) Periodic structural models for FeNC and FeNSC materials. The **FeNC1** and **FeNC2** are for FeNC and **FeNSC1** and **FeNSC2** are for FeNSC. (**b**) Mechanisms and energy profiles for the four-electron oxidation of TMB by O_2 on the FeN_4 site. **FeNC1** is illustrated as an example. The chemical components contained at each point on the energy curve are labeled below the catalytic cycle. (**c**) Band structure and PDOS for the four models. The d-band centers are labeled on the PDOS panels. (d) Isosurfaces and values for the differential charge densities of $\rho_{def,Fe}$ and $\rho_{def,OOH}$.

Applications of ROS regulation in task-specific catalytic reactions by FeNC and FeNSC.

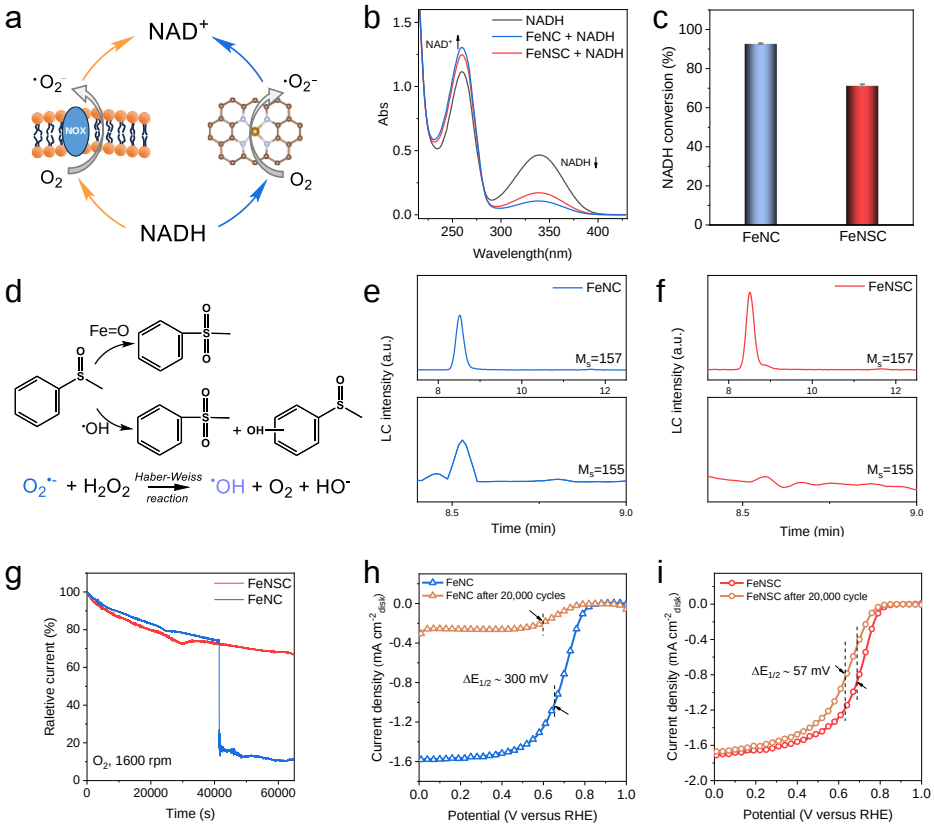

Figure 5. Application scenario with different free ROS demanding. (a) Scheme of NADH oxidation catalyzed by $\bullet O_2^-$ from natural electron transport chain or FeNC; (b) UV-vis absorption for NADH oxidation in the presence of FeNC and FeNSC; (c) NADH conversion rate in NADH oxidation reaction catalyzed by FeNC and FeNSC; (d) Oxidation of methyl phenyl sulfoxide (PMSO) catalyzed by Fe=O (bound ROS) to form sulfoxide and by •OH (free ROS) to yield sulfoxide and hydroxylation; Positive (M_s=157) and negative (M_s=155) liquid chromatography-tandem mass spectrometry (LC-MS) spectra of the supernatant of PMSO oxidation products catalyzed by (e) FeNC and (f) FeNSC; (g) Long-term stability assessment by chronoamperometry over FeNC and FeNSC in O_2-saturated 0.5m H_2SO_4 solution at a potential of 0.6 V; Initial stability results of (h) FeNC and (i) FeNSC by cycling the potentials (0.6–1.0 V, 20,000 cycles) in O_2-saturated 0.5 M H_2SO_4.

From the above results, it is discussed that the Fe-N coordination environment could be regulated by rational doping S atom, which strengthened the absorption of ROS intermediate on catalysts thus forming bound ROS and eliminating the generation of free ROS. This tunability to activate molecular oxygen encourages us to apply FeNC and FeNSC in task-specific reactions requiring discriminative free ROS or bound ROS.

NADH and NAD^+ are essential redox cofactors in the electron transport chain of metabolism. As known, $\bullet O_2^-$ could disrupt the NADH/NAD^+ balance state and promote the rapid oxidation of NADH.[28] Along this line, the catalytic performance of FeNC and FeNSC on NADH oxidation was evaluated by UV−vis spectroscopy. As shown in Figure 5b, the characteristic absorption peak at 340 nm for NADH decreased along with the increase of the absorption peak at 260 nm for NAD^+, indicating the conversion of NADH to NAD^+. Interestingly, FeNC revealed a much more efficient conversion rate of NADH (92 %) than FeNSC (71 %) in 4 h (Figure 5c). Thus, FeNC exhibited evident favorable activity in $\bullet O_2^-$ engaged oxidation of NADH.

In contrast to the utilizability of $\bullet O_2^-$ in NADH oxidation reaction, the indistinguishability of free ROS release usually hinders their catalytic specificity. For instance, methyl phenyl sulfoxide (PMSO) oxidation is an important reaction on pharmaceutical intermediates synthesis and industrial wastewater treatment, in which, Bound *O species can selectively convert PMSO to sulfone, whereas free ROS such as $\bullet$OH would convert PMSO to sulfone and hydroxylated sulfoxide.[53] Electrosprayionization-MS (ESI-MS) was first carried out to detect the catalytic oxidation product of PMSO. After oxidation, an additional fragment of sulfone was observed at m/z=157 using FeNSC (Figure S11). Then, positive ion liquid chromatography-tandem mass spectrometry (LC-MS) was utilized to quantify sulfone yield. As depicted in figure 5e, f, FeNSC shows a much stronger intensity than FeNC, indicting the more abundant Fe=O species presented in FeNSC. To enlarge the production of $\bullet$OH, H_2O_2 was introduced

based on the Haber-Weiss reaction in the presence of $\bullet O_2^-$ ($\bullet O_2^- + H_2O_2 \rightarrow \bullet OH + O_2 + HO^-$). Due to the same molecular weight of sulfone and hydroxylated sulfoxide, negative ion liquid chromatography-tandem mass spectrometry was applied to get further information on their products. As seen in Figure 5e, f, exclusive characteristic peak of hydroxylated sulfoxide at m/z=155 only appeared in FeNC-catalyzed reaction. The above catalytic reactions clearly demonstrate the significant role of Fe-N_4 second-shell coordination engineering, where the rational design of active site electronic environment can boost the reaction selectivity.

We then investigated the effect of free ROS regulation in electrocatalytic oxidation reaction. The design of durable oxygen reduction electrocatalysts for fuel cells is of paramount significance in modern society. Fe-N-C arouse increasing attention since 1960s as promising alternatives of platinum-based electrocatalysts.[21, 54] However, the stability of Fe-N-C as electrocatalysts have suffered from the undesirable free ROS release, particularly in acidic environment. Free ROS would cause the deteriorating performance of Fe-N-C by the oxidation of carbon to CO_2, which further lead to the demetallation of metal active sites or the formation of oxygen functional groups to greatly decrease the catalytic performance of catalysts.[7] Encouraged by the abundant $\bullet O_2^-$ species monitored in oxidase-like process of FeNC and the outstanding Fe=O efficiency of FeNSC without free ROS release, we deduce the regulation on free/bound ROS species could have a great impact on their stability. To this end, chronoamperometric measurements was first employed to evaluate the durability of the Fe-N-Cs in O_2-saturated 0.5m H_2SO_4 solution. After 60,000s, the FeNSC suffered a 30% loss of its initial current density, whereas the FeNC exhibited a sharp decline of 90% activity loss. (Figure 5g). The rotation ring disk electrode (RRDE) technique was also employed to evaluate the durability of the Fe-N-Cs. We subjected FeNSC and FeNC to a continuous voltammetry cycling process for 20,000 cycles in an O_2-saturated 0.5 M H_2SO_4 solution, as seen in

Figure 5h, after 20000 cycles, the ORR activity of FeNC demonstrated a significant decline after cycling by ca. 300 mV in the half-wave potential shifting to a more negative potential than that of the pristine FeNC. In comparison, FeNSC exhibited a much smaller activity loss after 20,000 cycles, with the half-wave potential shifting by around 57 mV (Figure 5i). These durability tests illustrate the regulation on ROS species by engineering the second-shell coordination configuration of FeN_4 center greatly enhance the stability in electrocatalysis.

Conclusion

In summary, we proposed single-atom nanozymes with distinct FeN_4 moieties to address the regulation of free ROS formation. Inspired from the refined hierarchical structures of CYPs with tetrapyrrolic FeN_4 active sites and S-containing ligand, FeNSC exhibited 2.4-fold oxidase-like velocity than FeNC towards TMB, whereas only 17 % free ROS ($\bullet O_2^-$) release was detected in FeNSC compared to FeNC. The catalytic mechanism of FeNC mainly followed the conventional free ROS pathway, in which $\bullet O_2^-$ served as an intermediate. Whereas the catalytic mechanism of FeNSC mainly followed the bound ROS (high iron-oxo) pathway, in which Fe-*O served as an intermediate. The comprehensive experiments and DFT calculations further proved that the second shell S-doping significantly altered the electronic structure of FeN_4 sites, leading to an increase of electron density at Fermi level and the enhanced electron transfer from active sites to the key intermediate *OOH, thereby determining the type of ROS in aerobic oxidation process. As a result, the highly biomimetic catalytic mechanism of Fe-N-C made it feasible to regulate free ROS by fine tuning the FeN_4 coordination environment. As proof-of concept applications, FeNC exhibits favorable activity in $\bullet O_2^-$ engaged oxidation of NADH, while FeNSC possesses superior performance in O* mediated selective

oxidation of organic sulfoxide. Furthermore, FeNSC with negligible •O_2^- release is used as model system to improve the stability of ORR electrocatalysis. This work not only provides fundamental insights into the regulation of ROS generation by single-atom nanozymes but also demonstrates an example of achieving reaction activity, selectivity and stability through mimicking the spatial architecture of natural enzyme.

Acknowledgments

This work was supported by the National Natural Science Foundation of China (22174014 and 22074015), and Gan Poyang talents support program, academic and technical leaders of major disciplines (20232BCJ23014).

References

1. Vander Heiden, M. G.; Cantley, L. C.; Thompson, C. B., Understanding the Warburg Effect: The Metabolic Requirements of Cell Proliferation. *Science* **2009,** *324* (5930), 1029-1033.
2. Gorrini, C.; Harris, I. S.; Mak, T. W., Modulation of oxidative stress as an anticancer strategy. *Nat. Rev. Drug Discov.* **2013,** *12* (12), 931-947.
3. Zorov, D. B.; Juhaszova, M.; Sollott, S. J., Mitochondrial Reactive Oxygen Species (ROS) and ROS-Induced ROS Release. *Physiol. Rev.* **2014,** *94* (3), 909-950.
4. Yang, B.; Chen, Y.; Shi, J., Reactive Oxygen Species (ROS)-Based Nanomedicine. *Chem. Rev.* **2019,** *119* (8), 4881-4985.
5. Schieber, M.; Chandel, Navdeep S., ROS Function in Redox Signaling and Oxidative Stress. *Curr. Biol.* **2014,** *24* (10), R453-R462.
6. Sies, H.; Berndt, C.; Jones, D. P., Oxidative Stress. *Annu. Rev. Biochem.* **2017,** *86* (1), 715-748.
7. Xie, H.; Xie, X.; Hu, G.; Prabhakaran, V.; Saha, S.; Gonzalez-Lopez, L.; Phakatkar, A. H.; Hong, M.; Wu, M.; Shahbazian-Yassar, R.; Ramani, V.; Al-Sheikhly, M. I.; Jiang, D.-e.; Shao, Y.; Hu, L., Ta–TiOx nanoparticles as radical scavengers to improve the durability of Fe–N–C oxygen reduction catalysts. *Nat. Energy* **2022,** *7* (3), 281-289.
8. Shao, Y.; Dodelet, J. P.; Wu, G.; Zelenay, P., PGM-Free Cathode Catalysts for PEM Fuel Cells: A Mini-Review on Stability Challenges. *Adv. Mat.* **2019,** *31* (31), e1807615.
9. Sun, H.; Lang, Z.; Zhao, Y.; Zhao, X.; Qiu, T.; Hong, Q.; Wei, K.; Tan, H.; Kang, Z.; Li, Y., Copper-Bridged Tetrakis(4-ethynylphenyl)ethene Aggregates with Photo-Regulated 1O2 and O2.− Generation for Selective Photocatalytic Aerobic Oxidation. *Angew. Chem. Int. Ed.* **2022,** *61*

(29), e202202914

10. Qian, Y.; Li, D.; Han, Y.; Jiang, H.-L., Photocatalytic Molecular Oxygen Activation by Regulating Excitonic Effects in Covalent Organic Frameworks. *J. Am. Chem. Soc.* **2020,** *142* (49), 20763-20771.
11. Yuan, J. P.; Guan, Z. J.; Lin, H. Y.; Yan, B.; Liu, K. K.; Zhou, H. C.; Fang, Y., Modeling the Enzyme Specificity by Molecular Cages through Regulating Reactive Oxygen Species Evolution. *Angew. Chem. Int. Ed.* **2023,** *62* (31), e202303896.
12. Xie, X.; He, C.; Li, B.; He, Y.; Cullen, D. A.; Wegener, E. C.; Kropf, A. J.; Martinez, U.; Cheng, Y.; Engelhard, M. H.; Bowden, M. E.; Song, M.; Lemmon, T.; Li, X. S.; Nie, Z.; Liu, J.; Myers, D. J.; Zelenay, P.; Wang, G.; Wu, G.; Ramani, V.; Shao, Y., Performance enhancement and degradation mechanism identification of a single-atom Co–N–C catalyst for proton exchange membrane fuel cells. *Nat. Catal.* **2020,** *3* (12), 1044-1054.
13. Bates, J. S.; Johnson, M. R.; Khamespanah, F.; Root, T. W.; Stahl, S. S., Heterogeneous M-N-C Catalysts for Aerobic Oxidation Reactions: Lessons from Oxygen Reduction Electrocatalysts. *Chem. Rev.* **2022,** *123* (9), 6233-6256.
14. Peng, C.; Pang, R.; Li, J.; Wang, E., Current Advances on the Single-Atom Nanozyme and Its Bioapplications. *Adv. Mat.* **2023**, 2211724.
15. Ji, S. F.; Jiang, B.; Hao, H. G.; Chen, Y. J.; Dong, J. C.; Mao, Y.; Zhang, Z. D.; Gao, R.; Chen, W. X.; Zhang, R. F.; Liang, Q.; Li, H. J.; Liu, S. H.; Wang, Y.; Zhang, Q. H.; Gu, L.; Duan, D. M.; Liang, M. M.; Wang, D. S.; Yan, X. Y.; Li, Y. D., Matching the kinetics of natural enzymes with a single-atom iron nanozyme. *Nat. Catal.* **2021,** *4* (5), 407-417.
16. Jiao, L.; Xu, W.; Zhang, Y.; Wu, Y.; Gu, W.; Ge, X.; Chen, B.; Zhu, C.; Guo, S., Boron-doped Fe-N-C single-atom nanozymes specifically boost peroxidase-like activity. *Nano Today* **2020,** *35*, 100971.
17. Ma, C. B.; Xu, Y.; Wu, L.; Wang, Q.; Zheng, J. J.; Ren, G.; Wang, X.; Gao, X.; Zhou, M.; Wang, M.; Wei, H., Guided Synthesis of a Mo/Zn Dual Single-Atom Nanozyme with Synergistic Effect and Peroxidase-like Activity. *Angew. Chem. Int. Ed.* **2022,** *61* (25), e202116170
18. Huang, L.; Chen, J. X.; Gan, L. F.; Wang, J.; Dong, S. J., Single-atom nanozymes. *Sci. Adv.* **2019,** *5* (5), eaav5490.
19. Wang, H.; Yang, T.; Wang, J.; Zhou, Z.; Pei, Z.; Zhao, S., Coordination engineering in single-site catalysts: General principles, characterizations, and recent advances. *Chem* **2024,** *10* (1), 48-85.
20. Zhu, X.; Wu, J.; Liu, R.; Xiang, H.; Zhang, W.; Chang, Q.; Wang, S.; Jiang, R.; Zhao, F.; Li, Q.; Huang, L.; Yan, L.; Zhao, Y., Engineering Single-Atom Iron Nanozymes with Radiation-Enhanced Self-Cascade Catalysis and Self-Supplied H2O2 for Radio-enzymatic Therapy. *ACS Nano* **2022,** *16* (11), 18849-18862.
21. Liu, S.; Li, C.; Zachman, M. J.; Zeng, Y.; Yu, H.; Li, B.; Wang, M.; Braaten, J.; Liu, J.; Meyer, H. M.; Lucero, M.; Kropf, A. J.; Alp, E. E.; Gong, Q.; Shi, Q.; Feng, Z.; Xu, H.; Wang, G.; Myers, D. J.; Xie, J.; Cullen, D. A.; Litster, S.; Wu, G., Atomically dispersed iron sites with a nitrogen–carbon coating as highly active and durable oxygen reduction catalysts for fuel cells. *Nat. Energy* **2022,** *7* (7), 652-663.
22. Jiao, L.; Wu, J.; Zhong, H.; Zhang, Y.; Xu, W.; Wu, Y.; Chen, Y.; Yan, H.; Zhang, Q.; Gu, W.; Gu, L.; Beckman, S. P.; Huang, L.; Zhu, C., Densely Isolated FeN4 Sites for Peroxidase Mimicking. *ACS Catal.* **2020,** *10* (11), 6422-6429.

23. Zhang, R. F.; Xue, B.; Tao, Y. H.; Zhao, H. Q.; Zhang, Z. X.; Wang, X. N.; Zhou, X. Y.; Jiang, B.; Yang, Z. L.; Yan, X. Y.; Fan, K. L., Edge-site Engineering of Defective Fe-N4 nanozymes with Boosted Catalase-like Performance for Retinal Vasculopathies. *Adv. Mat.* **2022,** *34* (39), e2205324.
24. Zhang, L.; Jiang, X.; Zhong, Z.; Tian, L.; Sun, Q.; Cui, Y.; Lu, X.; Zou, J.-P.; Luo, S., Carbon Nitride Supported High-Loading Fe Single-Atom Catalyst for Activating of Peroxymonosulfate to Generate 1O2 with 100% Selectivity. *Angew. Chem. Int. Ed.* **2021,** *60* (40), 21751-21755.
25. Ma, W.; Mao, J.; He, C.-T.; Shao, L.; Liu, J.; Wang, M.; Yu, P.; Mao, L., Highly selective generation of singlet oxygen from dioxygen with atomically dispersed catalysts. *Chem. Sci.* **2022,** *13* (19), 5606-5615.
26. Cao, S. J.; Zhao, Z. Y.; Zheng, Y. J.; Wu, Z. H.; Ma, T.; Zhu, B. H.; Yang, C. D.; Xiang, X.; Ma, L.; Han, X. L.; Wang, Y.; Guo, Q. Y.; Qiu, L.; Cheng, C., A Library of ROS-Catalytic Metalloenzyme Mimics with Atomic Metal Centers. *Adv. Mat.* **2022,** *34* (16), e2200255.
27. Huo, M. F.; Wang, L. Y.; Wang, Y. W.; Chen, Y.; Shi, J. L., Nanocatalytic Tumor Therapy by Single-Atom Catalysts. *ACS Nano* **2019,** *13* (2), 2643-2653.
28. Wu, D.; Li, J.; Xu, S.; Xie, Q.; Pan, Y.; Liu, X.; Ma, R.; Zheng, H.; Gao, M.; Wang, W.; Li, J.; Cai, X.; Jaouen, F.; Li, R., Engineering Fe–N Doped Graphene to Mimic Biological Functions of NADPH Oxidase in Cells. *J. Am. Chem. Soc.* **2020,** *142* (46), 19602-19610.
29. Chen, D.; Xia, Z.; Guo, Z.; Gou, W.; Zhao, J.; Zhou, X.; Tan, X.; Li, W.; Zhao, S.; Tian, Z.; Qu, Y., Bioinspired porous three-coordinated single-atom Fe nanozyme with oxidase-like activity for tumor visual identification via glutathione. *Nat. Commun.* **2023,** *14* (1), 7127.
30. Chen, X. H.; Zhao, L. F.; Wu, K. Q.; Yang, H.; Zhou, Q.; Xu, Y.; Zheng, Y. J.; Shen, Y. F.; Liu, S. Q.; Zhang, Y. J., Bound oxygen-atom transfer endows peroxidase-mimic M-N-C with high substrate selectivity. *Chem. Sci.* **2021,** *12* (25), 8865-8871.
31. Jiao, L.; Kang, Y.; Chen, Y.; Wu, N.; Wu, Y.; Xu, W.; Wei, X.; Wang, H.; Gu, W.; Zheng, L.; Song, W.; Zhu, C., Unsymmetrically coordinated single Fe-N3S1 sites mimic the function of peroxidase. *Nano Today* **2021,** *40*, 101261.
32. Wan, K. W.; Jiang, B.; Tan, T.; Wang, H.; Liang, M. M., Surface-Mediated Production of Complexed •OH Radicals and Fe O Species as a Mechanism for Iron Oxide Peroxidase-Like Nanozymes. *Small* **2022**, e2204372.
33. Hou, K.; Börgel, J.; Jiang, H. Z. H.; SantaLucia, D. J.; Kwon, H.; Zhuang, H.; Chakarawet, K.; Rohde, R. C.; Taylor, J. W.; Dun, C.; Paley, M. V.; Turkiewicz, A. B.; Park, J. G.; Mao, H.; Zhu, Z.; Alp, E. E.; Zhao, J.; Hu, M. Y.; Lavina, B.; Peredkov, S.; Lv, X.; Oktawiec, J.; Meihaus, K. R.; Pantazis, D. A.; Vandone, M.; Colombo, V.; Bill, E.; Urban, J. J.; Britt, R. D.; Grandjean, F.; Long, G. J.; DeBeer, S.; Neese, F.; Reimer, J. A.; Long, J. R., Reactive high-spin iron(IV)-oxo sites through dioxygen activation in a metal–organic framework. *Science* **2023,** *382* (6670), 547-553.
34. Halliwell, B., Reactive Species and Antioxidants. Redox Biology Is a Fundamental Theme of Aerobic Life. *Plant Physiol.* **2006,** *141* (2), 312-322.
35. Huang, X. Y.; Groves, J. T., Oxygen Activation and Radical Transformations in Heme Proteins and Metalloporphyrins. *Chem. Rev.* **2018,** *118* (5), 2491-2553.
36. Que, L.; Tolman, W. B., Biologically inspired oxidation catalysis. *Nature* **2008,** *455* (7211), 333-340.
37. Liu, W.; Chen, Q.; Wu, J.; Zhang, F.; Han, L.; Liu, J.; Zhang, H.; Hao, Z.; Shi, E.; Sun, Y.; Zhang, R.; Wang, Y.; Zhang, L., Asymmetric Coordination of Iron Single-Atom Nanozymes with Efficient

Self-Cascade Catalysis for Ferroptosis Therapy. *Adv. Funct. Mater.* **2023**, 2312308.

38. Yu, L.; Li, Y.; Ruan, Y., Dynamic Control of Sacrificial Bond Transformation in the Fe−N−C Single-Atom Catalyst for Molecular Oxygen Reduction. *Angew. Chem. Int. Ed.* **2021,** *60* (48), 25296-25301.
39. Yuan, L. J.; Liu, B.; Shen, L. x.; Dai, Y. K.; Li, Q.; Liu, C.; Gong, W.; Sui, X. L.; Wang, Z. B., d-Orbital Electron Delocalization Realized by Axial Fe4C Atomic Clusters Delivers High-Performance Fe–N–C Catalysts for Oxygen Reduction Reaction. *Adv. Mat.* **2023,** *35* (39), 2305945.
40. Xiong, Y.; Li, H.; Liu, C.; Zheng, L.; Liu, C.; Wang, J. O.; Liu, S.; Han, Y.; Gu, L.; Qian, J.; Wang, D., Single-Atom Fe Catalysts for Fenton-Like Reactions: Roles of Different N Species. *Adv. Mat.* **2022,** *34* (17), 2110653
41. Ni, L.; Gallenkamp, C.; Wagner, S.; Bill, E.; Krewald, V.; Kramm, U. I., Identification of the Catalytically Dominant Iron Environment in Iron- and Nitrogen-Doped Carbon Catalysts for the Oxygen Reduction Reaction. *J. Am. Chem. Soc.* **2022,** *144* (37), 16827-16840.
42. Daniel, G.; Mazzucato, M.; Brandiele, R.; De Lazzari, L.; Badocco, D.; Pastore, P.; Kosmala, T.; Granozzi, G.; Durante, C., Sulfur Doping versus Hierarchical Pore Structure: The Dominating Effect on the Fe–N–C Site Density, Activity, and Selectivity in Oxygen Reduction Reaction Electrocatalysis. *ACS Appl. Mater. Inter.* **2021,** *13* (36), 42693-42705.
43. Zitolo, A.; Ranjbar-Sahraie, N.; Mineva, T.; Li, J.; Jia, Q.; Stamatin, S.; Harrington, G. F.; Lyth, S. M.; Krtil, P.; Mukerjee, S.; Fonda, E.; Jaouen, F., Identification of catalytic sites in cobalt-nitrogen-carbon materials for the oxygen reduction reaction. *Nat. Commun.* **2017,** *8* (1).
44. Hannay, C.; Hubin-Franskin, M.-J.; Grandjean, F.; Briois, V.; Polian, A.; Trofimenko, S.; Long, G. J., X-ray Absorption Spectroscopic Study of the Temperature and Pressure Dependence of the Electronic Spin States in Several Iron(II) and Cobalt(II) Tris(pyrazolyl)borate Complexes. *Inorg. Chem.* **1997,** *36* (24), 5580-5588.
45. Zhang, H.; Wang, P.; Zhang, J.; Sun, Q.; He, Q.; He, X.; Chen, H.; Ji, H., Boosting the Catalase-Like Activity of SAzymes via Facile Tuning of the Distances between Neighboring Atoms in Single-Iron Sites. *Angew. Chem. Int. Ed.* **2023**, e202316779.
46. Gao, L. Z.; Zhuang, J.; Nie, L.; Zhang, J. B.; Zhang, Y.; Gu, N.; Wang, T. H.; Feng, J.; Yang, D. L.; Perrett, S.; Yan, X. Y., Intrinsic peroxidase-like activity of ferromagnetic nanoparticles. *Nature Nanotech.* **2007,** *2* (9), 577-583.
47. Xu, Y.; Xue, J.; Zhou, Q.; Zheng, Y. J.; Chen, X. H.; Liu, S. Q.; Shen, Y. F.; Zhang, Y. J., The Fe-N-C Nanozyme with Both Accelerated and Inhibited Biocatalytic Activities Capable of Accessing Drug–Drug Interactions. *Angew. Chem. Int. Ed.* **2020,** *59* (34), 14498-14503.
48. Cai, S.; Liu, J.; Ding, J.; Fu, Z.; Li, H.; Xiong, Y.; Lian, Z.; Yang, R.; Chen, C., Tumor-Microenvironment-Responsive Cascade Reactions by a Cobalt-Single-Atom Nanozyme for Synergistic Nanocatalytic Chemotherapy. *Angew. Chem. Int. Ed.* **2022**, e202204502.
49. Yang, Y.; Banerjee, G.; Brudvig, G. W.; Kim, J.-H.; Pignatello, J. J., Oxidation of Organic Compounds in Water by Unactivated Peroxymonosulfate. *Environ. Sci. Technol.* **2018,** *52* (10), 5911-5919.
50. Fridovich, I., Superoxide Radical: An Endogenous Toxicant. *Annu. Rev. Pharmacol.* **1983,** *23* (1), 239-257.
51. Watanabe, Y.; Nakajima, H.; Ueno, T., Reactivities of Oxo and Peroxo Intermediates Studied by Hemoprotein Mutants. *Acc. Chem. Res.* **2007,** *40* (7), 554-562.

52. Christoforidis, K. C.; Louloudi, M.; Milaeva, E. R.; Sanakis, Y.; Deligiannakis, Y., EPR study of a novel [Fe–porphyrin] catalyst. *Mol. Phys.* **2010,** *105* (15-16), 2185-2194.
53. Chen, L.; Wang, S.; Yang, Z.; Qian, J.; Pan, B., Selective interfacial oxidation of organic pollutants in Fenton-like system mediated by Fe(III)-adsorbed carbon nanotubes. *Appl. Catal. B* **2021,** *292*, 120193.
54. Menga, D.; Low, J. L.; Li, Y.-S.; Arčon, I.; Koyutürk, B.; Wagner, F.; Ruiz-Zepeda, F.; Gaberšček, M.; Paulus, B.; Fellinger, T.-P., Resolving the Dilemma of Fe–N–C Catalysts by the Selective Synthesis of Tetrapyrrolic Active Sites via an Imprinting Strategy. *J. Am. Chem. Soc.* **2021,** *143* (43), 18010-18019.